

Relativistic and Electromagnetic Molecular Dynamics Simulations for a Carbon–Gold Nanotube Accelerator

Motohiko Tanaka, and Masakatsu Murakami¹

Graduate School of Engineering, Chubu University, Kasugai 487-8501, Japan

¹Institute of Laser Engineering, Osaka University, Suita 565-0871, Japan

October 29, 2019

Abstract

Relativistic molecular dynamics are described by the real charge and mass of particles. Coulomb potential is collected in the infinite space, and the electromagnetic fields are solved in the coordinate space. The longitudinal and transverse electric fields are separated, which is a good approximation for a short time periods. For a numerical application, a nanotube accelerator under an $E \times B$ pulse is performed. Positive ions are accelerated in the parallel direction, whereas the electrons proceed in the perpendicular direction in the relativistic velocities. The energy of multiple gold ions is about 30 MeV, and the energy efficiency is 1% at $10^{22}\text{W}/\text{cm}^2$. The electromagnetic field effects are examined in different spatial scales, which are satisfactory in molecular dynamics simulations.

Keywords: molecular dynamics simulation, Coulomb potential, longitudinal and transverse fields, nanoscale materials, plasma production by laser beam

1 Introduction

Ion accelerations driven by ultraintense and ultrashort laser pulses have been studied over the past two decades. Positive ion beams have wide applications such as tomography, cancer therapy [1], compact neutron sources [2], and ion-driven fast ignition for medicine [3]. To practically use accelerated ions, it is crucial to produce high-quality beams, which are monoenergetic and collimated [4, 5, 6]. Laser-driven ion acceleration has been reviewed in the literature [7].

A temperature of 10^{10}K and a pulse duration of 10 fs are proposed for MeV-range accelerator physics and applications. A molecular dynamics simulation suggested that a nanometer-sized nanotube can generate a quasi-monochromatic and directional beam of protons and carbon ions in the MeV energy range [8]. Additionally, a gold coating can be chemically adsorbed to the monolayer of carbon atoms, which comprise the carbon nanotube [9]. Low- Z materials such as hydrogen and carbon are fully ionized, while materials such as gold have mid-range ionization states $Z \leq 25$ at laser intensities of $\leq 10^{18}\text{W}/\text{cm}^2$ [10]. Increasing the irradiated laser intensity by several orders of magnitude will be an

interesting challenge as both the energy and energy efficiency must be increased above $10^{18}\text{W}/\text{cm}^2$.

Such physics and chemistry research has been greatly advanced due to large parallel machines. Although advances were once limited to the electrostatic area, the Coulomb potential is simply periodic or makes use of the Ewald method for high accuracy [11]. For the latter, the code is $\exp(-(\gamma r)^2)/r$ in the short range, while the charge density with aliasing sum factor is convolved by a Fourier transform the long range. These research fields are involved in the microwave heating of water and ice [12], the microwave heating of magnetite [13], the charge inversion and electrophoresis phenomena [14, 15, 16], DNA translocation in the nanopore [17], and macromolecules of polyampholyte [18]. Additionally, the simulation code in the electromagnetic area was solved in coordinate space and for periodic conditions [19]. The code was applied for space physics [20]. However, for electromagnetic phenomena in an unbound space such as in long-range forces, all particles must be summed in the infinite volume [21]. In principle, the plasma approximation for a nearly uniform density using particle-in-cell codes is not applicable.

Incidentally in the aforementioned work, a carbon nanotube was used in the relativistic molecular dynamics simulations. On the one hand, the simulations used the electrostatic approximation. On the other hand, the mass of the proton to electron ratio was used as 100, which is insufficient to separate the ion and electron dynamics. Fortunately, molecular dynamics simulations using today's technology are powerful, and real mass and charge particles can be considered with electromagnetic effects. Simulations can use the atomic unit of an element (e.g., proton= 1, carbon= 12, and gold= 197), and the electron of $(1836)^{-1}$. The scalings of these ions and electrons can be addressed without adjustments.

The rest of this paper is organized on follows. In Sec.2, the methodology of molecular dynamics for relativistic and electromagnetic field simulations is described. A concise procedure, which separates the longitudinal and transverse electric fields, is a good approximation of small-scale phenomena. Section 3 describes the numerical application of the molecular dynamics code. Protons, carbons, golds, and electrons are used at their real mass ratios, where the applied $E \times B$ Gaussian pulse in the time and space is given as $(\omega t - k_y y)$. The carbon nanotube is accelerated in the parallel and perpendicular directions for ions and electrons, respectively, and the energy efficiency is about 1% at $10^{22}\text{W}/\text{cm}^2$. Section 4 compares the present electromagnetic code to the previous electrostatic code. Finally Sec.5 summarizes the paper.

2 Methodology of Molecular Dynamics with Relativistic and Electromagnetic Field Simulations

2.1 Motion and Maxwell Field Equations

Solving the Newton equation of motion for position $\vec{r}(t)$ and velocity $\vec{v}(t)$ can realize time development in a system. Since particle positions are located in infinite space, the determination of the charged particles interactions must be highly accurate. The Coulomb potential is used in the equation of motion,

which is written as

$$\Phi_{Coul}(\vec{r}_i) = \sum_{j=1}^N q_i q_j / r_{ij}. \quad (1)$$

where q_i is the i^{th} particle charge, r_i is the position in the parallel (z) and lateral directions (x and y). The vector $r_{ij} = r_i - r_j$ is the displacement between the i^{th} and j^{th} particles. The sum of all possible combinations of particles must be specified.

Generally in nanometer crystals, particles have strong short-range interactions. These interactions can be represented by the Lennard-Jones potential, which is expressed as

$$\Phi(r_i, r_j) = \epsilon_{ij}[(\sigma_{ij}/r_{ij})^{12} - 2(\sigma_{ij}/r_{ij})^6]. \quad (2)$$

The short-range potential is repulsive if the distance between the two particles is small, but is attractive if the particle distance is larger than the equilibrium distance. The potential for carbon pairs has an equilibrium at $\sigma_{CC} = 1.421\text{\AA}$ and $\epsilon_{CC} = 4\text{eV}$ ($1\text{eV} = 1.602 \times 10^{-12}\text{erg}$). Hence, a solid six-membered network of nanotubes is created. The other ions are weakly dependent, and their potentials are assumed to be null, $\epsilon_{AuAu} = 0$. Actually, the depth of the carbon potential is about $T \approx 4 \times 10^4\text{K}$. Consequently, the short-range potential works to initially form a nanotube crystal. Within the 10-\AA pairs, the Coulomb and Lennard-Jones interactions are calculated at a small time step Δt , while the interactions beyond that range occur at $5\Delta t$.

The electromagnetic interactions in three-dimensional rectangular coordinates can be calculated by a set of Maxwell equations. Usually, the retarded potential is used for the special relativity[22, 23]. Although this potential is difficult to solve for a system with a large number of particles, such as $N > 10^5$ particles, the separation of the transverse and longitudinal electric fields can be approximated for small-scale phenomena. The physical process is contained in 100 nm of the accelerated nanotube where the light travels one-tenth of the period (about 0.3 fs) for an 800-nm sapphire laser.

For electromagnetic fields, finite coordinate grids are used, which define the transverse electric field $\vec{E}_T(\vec{r}, t)$, the longitudinal electric field $\vec{E}_L(\vec{r}, t)$, and the magnetic field $\vec{B}(\vec{r}, t)$. The key to solve the transverse \vec{E}_T and longitudinal \vec{E}_L electric fields is that the current density is orthonormal to the transverse \vec{j}_T and longitudinal \vec{j}_L currents. The longitudinal electric field is initially solved in the coordinate space by

$$\nabla \cdot \vec{E}_L(\vec{r}, t) = 4\pi \sum_{i=1}^N q_i S(\vec{r} - \vec{r}_i), \quad (3)$$

where the summation is taken over particles and $S(\vec{r})$ is prorated to nearby grids (the shape function is $S(\vec{0}) = 1$ and $S(\vec{r}) \rightarrow 0$ when $|\vec{r}| \gg \Delta x$). The transverse current can be separated from the longitudinal current, which is given by

$$\vec{j}_T = \vec{j} - (\vec{j} \cdot \vec{E}_L) / |\vec{E}_L|. \quad (4)$$

Here, the current density \vec{j} is summed over the charge and velocity of the particles as

$$\vec{j}(\vec{r}) = \sum_{i=1}^N q_i \vec{v}_i S(\vec{r} - \vec{r}_i). \quad (5)$$

In reality, the electromagnetic interactions are limited to the internal (coordinate) domain due to the available meshes from computer resources. (See Sec.4 for the numerical verification of electromagnetic effects.)

To define momentum \vec{p}_i , position \vec{r}_i , and velocity \vec{v}_i , the relativistic equation of motion is written as

$$d\vec{p}_i/dt = -\nabla \sum_{j=1}^N [q_i q_j / r_{ij} + \Phi(r_i, r_j)] + q_i [\vec{E}_T(\vec{r}_i, t) + (1/c) \vec{v}_i \times \vec{B}(\vec{r}_i, t)], \quad (6)$$

$$d\vec{r}_i/dt = \vec{v}_i, \quad \vec{p}_i = m_i \vec{v}_i / \sqrt{1 - (\vec{v}_i/c)^2}. \quad (7)$$

The longitudinal (electrostatic) terms in the first bracket (namely Eq.(1) and Eq.(2)) and the transverse (electromagnetic) terms in the second bracket in Eq.(6) are used. Here, m_i is the mass of the i^{th} particle, c is the speed of light, the symbol d/dt is the full time derivative, and ∇ is an operator $(\partial/\partial x, \partial/\partial y, \partial/\partial z)$. The second bracket is determined by the Maxwell equation, which is given as

$$(1/c) \partial \vec{B} / \partial t = -\nabla \times \vec{E}_T, \quad (8)$$

$$(1/c) \partial \vec{E}_T / \partial t = \nabla \times \vec{B} - (4\pi/c) \sum_{i=1}^N q_i \vec{v}_{T,i} S(\vec{r} - \vec{r}_i), \quad (9)$$

$$\nabla \cdot \vec{B} = 0, \quad (10)$$

with $\vec{B} = \vec{H}$ of plasmas in the CGS system. The $\partial/\partial t$ term is the round derivative of time, and the space operator of three dimensions, for example the electric field, is given by

$$\nabla \times \vec{E} = (\partial E_y / \partial z - \partial E_z / \partial y, \partial E_z / \partial x - \partial E_x / \partial z, \partial E_x / \partial y - \partial E_y / \partial x). \quad (11)$$

The \vec{E}_T and \vec{B} fields are the transverse electric and magnetic fields, respectively. The electric field \vec{E} is finally written by the sum of $(-\nabla \Phi_{Coul})$ and \vec{E}_T terms.

The internal grids have $M_x = M_y = 100$ and $M_z = 200$ cells centered at the origin. They amount $500 \times 500 \times 1000 \text{\AA}^3$ in $\vec{E}_T(\vec{r}_i)$ and $\vec{B}(\vec{r}_i)$ in the x, y and z directions. In the external regime, other components are null except for Φ_{Coul} in Eq.(1) and the drift terms $(E_{z,0}, B_{x,0})(\vec{r}, t)$. The Gaussian pulse with an 800-nm wavelength ($2.67 \times 10^{-15} \text{s}$) is induced from the negative y direction toward the origin at the speed of light. It decays in $\Delta Y = 2.8 \mu\text{m}$ in the y direction, namely $3.5 \times 800 \text{nm}$, and $\Delta X = 0.1 \mu\text{m}$ in the x, y directions as

$$\begin{aligned} E_{z,0}(\vec{r}, t) &= E_0 \sin(\omega t - k_y y) * f_n, \\ B_{x,0}(\vec{r}, t) &= B_0 \cos(\omega t - k_y y) * f_n, \end{aligned} \quad (12)$$

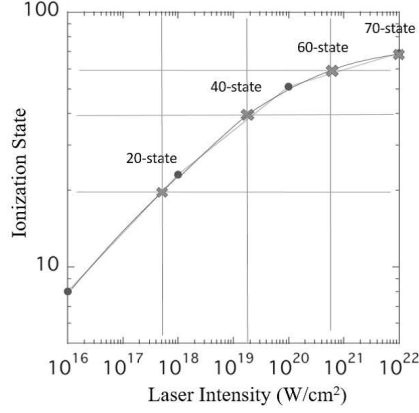


Figure 1: Laser intensity and ionization state of gold ions for $10^{16} - 10^{22} \text{W/cm}^2$.

and the slope f_n is

$$f_n = \exp[-((y - p_{xyz})^2/\Delta Y^2 + (x^2 + z^2)/\Delta X^2)]. \quad (13)$$

Here, the oscillation frequency is $\omega = ck_y$, $E_0 = B_0$, $p_{xyz} = (-3 + t/2.67 \times 10^{-15}) \times 800 \text{nmC}$ and the time step is $\Delta t = 5 \times 10^{-19} \text{s}$. The laser intensity $5 \times 10^{17} \text{W/cm}^2$ corresponds to the electric field $1.46 \times 10^{12} \text{V/m}$ in the MKS unit, which is $4.58 \times 10^7 \text{statV/cm}$ in the CGS unit. (Refer to the Appendix for the international system of units.)

2.2 Ionization state and Courant condition

The values studied in this simulation range between 10^{16}W/cm^2 to 10^{22}W/cm^2 . The carbon nanotube on the surface of the two-dimensional cylinder surface is about 15 nm (radial, diameter) and 30 nm (height, diameter). The gold ions are set by 2-Å positions outside of the accompanying carbon pairs. Moreover, inside the inner cylinder, the bulk, which has a 12-nm diameter and 27-nm full length (height), is uniformly filled with protons and electrons. The proton and carbon ions are fully ionized due to the high laser intensity. On the other hand, the gold ions are partially ionized, depending on the laser intensity [10], as depicted in Fig.1. Each run is assigned an ionization state, $Z_{is} = 20, 40, 60$, and 70, which are designated as Run A1, A2, A3, and A4, respectively.

The plasma contains: (i) carbon ions with six ionization states and 55,000 particles, (ii) gold ions as described above with 55,000 particles, (iii) protons with a single ionization state and 10,000 particles, and (iv) electrons with a negative single ionization state. The charge neutrality condition determines the number of electrons. Particles (4.1×10^5) are assigned as protons, carbons, golds, or electrons. The initial temperature of the particles is equal to null. The physical run time of a single cage is set to $t = 30 \text{ fs}$ for Run A4, but Run A1 to A3 are executed as long runs with $t = 41\text{--}45 \text{ fs}$. The particles without protons are executed at $t = 25 \text{ fs}$ for Run B.

To minimize the number of electrons, the electrons are disguised such that electrons are lumped together as super-electrons with a super-charge and mass of $e_\alpha = -\alpha e$ and $m_\alpha = \alpha m_e$. One super electron with $e_\alpha = -6e$ is assigned to

Table 1: The kinetic energy of the carbons, golds, protons and electrons (MeV) for the laser intensity in Runs A1 to A4 (W/cm^2). The energy efficiency of the golds over electrons (%) is also given.

Series	laser intensity	C	Au	Proton	elec	Efficiency
A1	5.0×10^{17}	0.30	0.55	0.082	0.032	64%
A2	1.7×10^{19}	0.76	6.0	0.21	0.53	25%
A3	6.0×10^{20}	0.83	14.0	0.23	6.7	3.1%
A4	1.0×10^{22}	1.35	21.2	0.55	36.9	0.76%

a carbon ion. For gold, one super electron with $e_\alpha = -5e$ is assigned to one-fourth of the gold ions for Run A1. In the same token, one super electron with $e_\alpha = -10e$ is assigned to one-fourth of the gold ions for Run A2, one electron $e_\alpha = -15e$ is assigned to one-fourth of the gold ions for Run A3, and one super electron with $e_\alpha = -70/4e$ is assigned to one-fourth of the gold ions for Run A4. A positive ion, namely a proton, carbon, or gold, is used as the independent normal particle.

The Courant-Friedrichs-Lewy condition must be satisfied for the numerical code to be stable for electromagnetic waves [24]. The time step Δt and grid interval Δx must be greater than the speed of light,

$$\Delta x / \Delta t > c, \quad (14)$$

otherwise the simulation blows up immediately for the explicit code. Thus, the following condition should be met,

$$\begin{aligned} \Delta x / \Delta t &= 5 \times 10^{-8} \text{cm} / 5 \times 10^{-19} \text{sec} \\ &= 1 \times 10^{11} \text{cm/sec} > c. \end{aligned} \quad (15)$$

@

The molecular dynamics simulation runs with the *allreduce* sum of MPI communications for the longitudinal electric field interaction. It is necessary to sum N by N particles because a high accuracy is desired with a minimal numerical error. The computation by the parallel machine FX100 (Fujitsu), for minimal case, runs per 52 ranks with 16 processors and 4.1×10^5 particles. It then consumes almost 70% of the computation time for the *mpi_allreduce* calculation, which requires about 24 h for the 5×10^4 time steps (equal the physical run of $25 \times 10^{-15} \text{s}$).

3 Carbon nanotube accelerator assisted by gold ions

3.1 Time developments of ions and electrons

Table 1 shows the results for Run A1 to A4, which have a laser intensity of 10^{16} – $10^{22} \text{W}/\text{cm}^2$. Each run is initiated with a Gaussian pulse at the leftward position $y = -3.5 \times 800 \text{ nm}$. A laser shot radiates the nanotube sideways from the lateral direction. Figure 2 depicts the laser intensity of $5.0 \times 10^{17} \text{W}/\text{cm}^2$

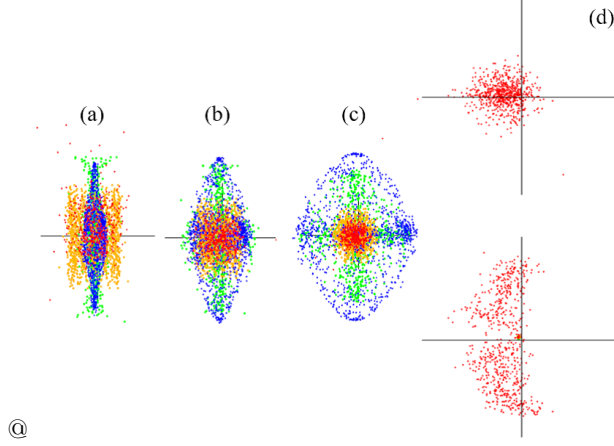


Figure 2: (Color) The time sequence of $5 \times 10^{17} \text{W/cm}^2$ (Run A1) for enlarged yz plot at (a) 13fs, (b) 20fs, (c) 45fs, and (d) for the reduced yx and yz plots, mostly of electrons, in 45fs. Protons are shown in blue, carbons by green, golds by gold, and electrons in red. The scales are $3.3 \times 10^{-6} \text{cm}$, $5.5 \times 10^{-6} \text{cm}$, $1.6 \times 10^{-5} \text{cm}$ in (a) to (c), respectively, and $9.4 \times 10^{-4} \text{cm}$ in two vertical plots (d).

for Run A1 with a time development of nanotube expansion of (a) 13 fs, (b) 20 fs, and (c) 45 fs for the yz plots, and (d) the reduced yx and yz plots with the electrons at 45 fs.

Laser irradiation induces a sudden rapid expansion of all ions. The antecedent protons (blue) are mainly accelerated in the parallel (z) direction of the nanotube cylinder, as seen in panels (a) - (c). The carbon (green) and gold ions (gold) follow the first protons like guard spears, and the acceleration of positive ions lasts for at least 45 fs. On the other hand, as the inverse of the electron mass is quite large m_e^{-1} (red), the electrons move about 100 times more for a larger space than the positive ions. Although the electrons are spread much wider than the ions, they are limited to $10 \mu\text{m}$ and are nearly confined in the $y < 0$ region in Run A1.

Figure 3 depicts the velocity distribution functions for Run A1. There is a main central peak, which extends with a tail formation for protons, carbons, and electrons at $5 \times 10^{17} \text{W/cm}^2$. The protons have positive and negative tails in V_{\parallel} . These tails are somewhat higher in the V_{\perp} direction. Carbon and gold ions have only thin tails, whereas electrons have thick tails in the V_{\parallel} direction.

At $1.7 \times 10^{19} \text{W/cm}^2$ (Run A2), carbon ions have a second peak in the geometry space compared to the first gold ions. The electrons develop a spiral shape outside the positive ions, and occupy both positive and negative z coordinates in the y direction. At $6 \times 10^{20} \text{W/cm}^2$ (Run A3), a large spiral, which resembles a semi-arc shape, occupies the negative z direction. The gold ion peak increases to 14.0 MeV, and the electrons have a second position at 6.7 MeV; carbon ions fall down to the third position. Regardless of the order, the carbon ions are the most important component because the six-membered cage of the nanotube must be supported initially.

At $1 \times 10^{22} \text{W/cm}^2$ (Fig.4, Run A4), the electrons are completely separated

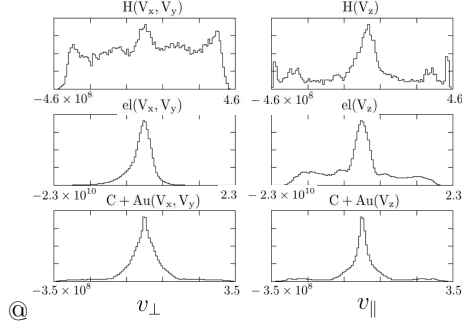


Figure 3: The velocity distribution functions of protons, electrons, and carbon plus gold ions for Run A1 (from the top to bottom panels, respectively). A time is 40fs for the perpendicular direction (V_x, V_y) (left), and the parallel direction V_z (right), with c the speed of light in cm/s.

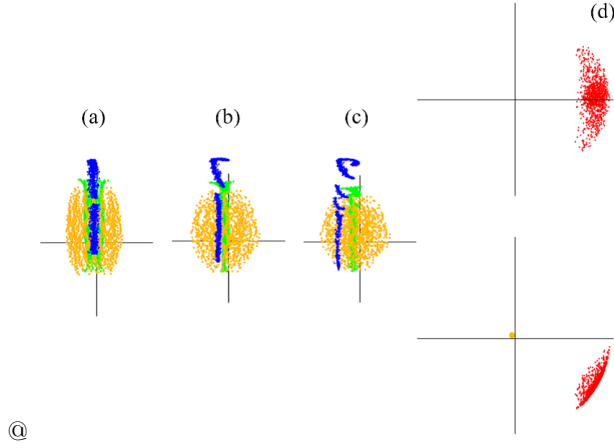


Figure 4: (Color) The time sequence of $1 \times 10^{22} \text{W/cm}^2$ (Run A4) for enlarged yz plots at (a) 5fs, (b) 11fs, (c) 30fs, and (d) for reduced yx and yz plots, mainly of electrons, at 30fs. Protons are shown in blue, carbons by green, golds by gold, and electrons in red. The scales are $5.5 \times 10^{-6} \text{cm}$, $1.2 \times 10^{-5} \text{cm}$ and $3.7 \times 10^{-5} \text{cm}$ in (a) to (c), respectively, and $7.4 \times 10^{-4} \text{cm}$ in two vertical plots (d).

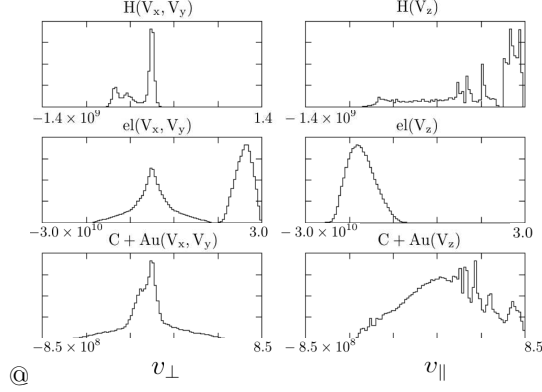


Figure 5: The velocity distribution functions of protons, electrons, and carbon plus gold ions for Run A4 (from the top to bottom panels, respectively). A time is 23fs for the perpendicular direction (V_x, V_y) (left), and the parallel direction V_z (right), with c the speed of light in cm/s.

from all the ions. They proceed in the $E \times B$ drift in the $y > 0$ direction. Their velocities are nearly 90% that of the speed of light. The time plot indicates that pulsation oscillations exist for the gold ions. Figure 5 shows the velocity distribution functions. Protons in the parallel direction have a velocity at 1.4×10^9 cm/s and are broadly distributed from the top and bottom portions, $\pm 4 \times 10^9$ cm/s. The carbon and gold ions have half the velocity of the protons. The population centered at 8×10^8 cm/s in the parallel direction is due to the carbon ions, while that centered at 3×10^8 cm/s is due to the gold ions. The electrons are relativistic and V_y is decentered at -2×10^{10} cm/s.

3.2 Behavior of energy and efficiency

The momentum and the energy of each particle reveal the acceleration behavior of plasma. The momentum of the species with N_s particles is defined by $W_{kin,s} = \sum_{i=1}^{N_s} (\vec{p}_i^2 / 2m_i)$, where the total momenta determine the course of the dynamical system. The separate behavior of the ions and electrons are highlighted, which are divided by N_s as $w_{kin,s} = \sum_{i=1}^{N_s} (\vec{p}_i^2 / 2m_i) / N_s$.

The energies of the gold ions, carbon ions, and protons increase monotonically in Run A1 (Fig.6(a)). The gold ions grow twice as fast as the carbon ions at 45 fs, and the electric interactions with these heavy ions are important. The growth of the protons is one order of magnitude smaller than that of heavy ions. The electrons become saturated around $t = 15$ fs, but their growth is half of that for the gold ions for Run A1. The energies on the average are 0.55 MeV for golds, 0.30 MeV for carbons, 0.082 MeV for protons, and 0.33 MeV for electrons.

Figure 6(b) shows the time change of the energy for Run A4. The energy of the electrons is 99% of the total energy as early as 3 fs. Its energy is as large as 37 MeV. The gold ions exhibit fast pulsation oscillations around 10 fs, which become saturated at 21 MeV and finally converge to two-thirds of the maximum level for 30 fs. The proton energy is fairly small because its mass is about 200^{-1} that of gold.

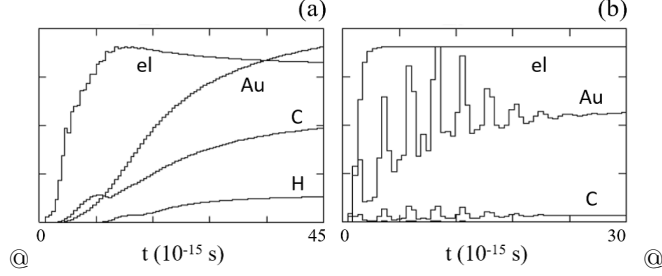


Figure 6: The time change of kinetic energy of the golds, carbons, protons, and electrons for (a) $5 \times 10^{17} \text{W/cm}^2$, and (b) $1 \times 10^{22} \text{W/cm}^2$. The maximum values are, (a) 0.55MeV for ions (C,Au,H), 0.33MeV for electrons, (b) 34.1MeV for ions, 36.9MeV for electrons, respectively.

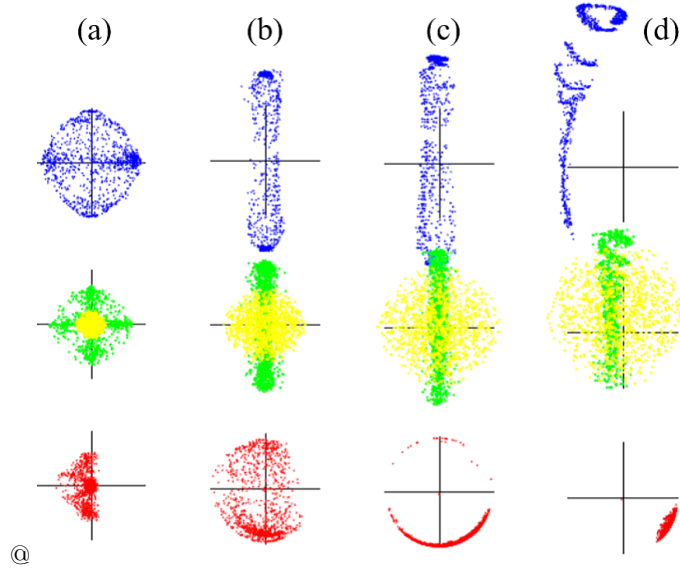


Figure 7: (Color) The 2D velocity plots of protons, carbons and golds, and electrons, from the top to bottom panels, respectively. The times for Run A1 to A4 are, (a) 45fs, (b) 35fs, (c) 35fs, and (d) 30fs. The plot scales are, 100 times in the top row (for protons, blue), 50 times in the middle row (for carbon, green, and gold, gold), and 1.5 times for the bottom row (for electrons, red).

Table 2: The carbon, gold and electron energies (MeV), and energy efficiency of the golds to electrons (%) for the number of golden layers within a nanotube. Quotation to Run A4 for the single cage (without protons) is shown as the first line.

Series	layers	C	Au	elec	Efficiency
A4	1	1.35	21.2	36.9	0.76%
B1	2	1.9	26.0	39.0	0.88%
B2	3	2.4	29.8	39.9	0.98%

Figure 7 compares the velocity distributions in the (V_y, V_z) space for Runs A1 - A4. For Run A1, the protons, carbon ions, and gold ions are symmetric in the first two rows of panel (a). However, the electrons in the third row occupy the leftward hemisphere V_y , and both the top and bottom parts in the direction V_z resemble a butterfly pattern. Run A2 in panel (b) is symmetric for the positive ions, but the electrons in the third row form a large arc in the entire $V_x - V_y$ space. For Run A3 in (c), the electrons form an antisymmetric arc, which appears quite large in the $V_z < 0$ regime. Finally, for Run A4 in (d), the pipe shape for the protons is totally antisymmetric after $t > 10$ fs, and the electrons exhibit a very large island in the fourth quadrant with $V_y > 0$.

The momentum elucidates the energy efficiency among the species. The momenta of Run A1 are 17.2%, 31.9%, 0.86%, and 50.1% for carbons, golds, protons, and electrons, respectively. These ions and electrons are almost equally divided, and the ratio of the gold to electron is $(\text{Au}/\text{electron}) = 64\%$. As the laser intensity increases between Run A2 to Run A3, the energy efficiency of the ions drops exponentially. The energy efficiency of the gold to electron for Run A3 becomes 3.1%. At the Run A4 intensity, the ratios are $4.8 \times 10^{-2}\%$, 0.77%, $3.5 \times 10^{-3}\%$, and 99.0% for carbons, golds, protons, and electrons, respectively. The ratio of gold to electron is $(\text{Au}/\text{electron}) = 0.76\%$. For the kinetic energy over the intensity $\geq 10^{20} \text{W}/\text{cm}^2$, the trend shows that the gold ions are approaching a parabolic sub-relativistic regime, which is compared to a linear relativistic regime for the electrons.

Good optimizations are incremented at $1 \times 10^{22} \text{W}/\text{cm}^2$ in Table 2. The $E \times B$ drift speed remains the same as before. The cylindrical single cage becomes more powerful when using a double or triple cage in Run B compared to the single cage in Run A. The rapid fast oscillations of gold ions of Runs B1 and B2 are subsidized by $t < 20$ fs, and the energy at the final time is about 70% of the maximum value at 10 fs. The final value for the double-stacked cylindrical cage is 26 MeV (Run B1, on the average), while that of the triple-stacked cylindrical cage is 29.5 MeV (Run B2). The calculated energy efficiencies for the double and triple-stacked cages are $(\text{Au}/\text{electron}) = 0.89\%$ and 0.97% , respectively.

4 Electromagnetic versus electrostatic field effects

The electromagnetic \vec{E} and \vec{B} fields in the present simulation and the electrostatic electric \vec{E}_L field in the old simulation are compared for the relativistic

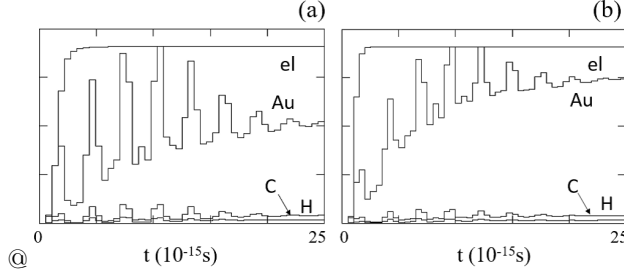


Figure 8: Comparison of the electrostatic simulation (Run A4 α , a) and the 2^3 times large simulation in the electromagnetic field (Run A4 β , b). For (a), the maximum and final kinetic energies are 39.6 MeV and 22.7 MeV for the gold ions, respectively. The maximum and final ones for (b) are 23.6 MeV and 19.4 MeV, respectively. The scales for the electrons are different whose maxima of the electrons are 37.2 MeV and 39.7 MeV in (a) and (b), respectively.

case 10^{22} W/cm^2 . The Gaussian pulse in the y direction is applied in common with three types of simulations below.

First, the electrostatic simulation with $\vec{E}_T = \vec{B} = 0$ is executed for the carbon nanotube accelerator (Fig.8(a)). The positive ions (protons and gold ions) are accelerated in the parallel direction, while the electrons are accelerated solely in the perpendicular direction. The proton distribution function of V_{\parallel} converges at $V_{\parallel, \text{top}} \approx 1.4 \times 10^9 \text{ cm/s}$. Pulsation oscillations occur for the 2.7-fs period for the gold ions, and its highest energy is 39.6 MeV. The final pulsation oscillation energies are 22.7 MeV for the gold ions and 37.2 MeV for the electrons.

Next, an electromagnetic simulation with a medium size, $M_x = M_y = 100$ and $M_z = 200$ cells, namely, the internal domain of $|x| \leq 250 \text{ \AA}$ and $|z| \leq 500 \text{ \AA}$, is described for Run A4. (The main parameters are described in Sec.3.) The proton distribution function of V_{\parallel} is widely distributed from the maximum positive to the negative parts (Fig.5). Although fast pulsation oscillations occur for the gold ions in the early phase, the top energy is 34.1 MeV at $t=10$ fs. The final energy of the gold ions is 21.0 MeV. The energy of the gold ions is much moderate compared with the electrostatic simulation above. The maximum energy of the electrons is 37 MeV because the rectangular box mostly covers the electromagnetic interactions.

The large-sized electromagnetic simulation is twice the size in each direction as the medium-sized one, $M_x = M_y = 200$ and $M_z = 400$ cells (Fig.8(b)). The electromagnetic interaction is well confined in the internal domain of $|x| \leq 500 \text{ \AA}$ and $|z| \leq 1000 \text{ \AA}$. The energy of the gold ions is found to be most moderated at 23.6 MeV for $t = 11.5$ fs, and the energy converges to a medium value of 19.4 MeV for the large-scale run. That of the electrons is 40 MeV.

Although the energy of the gold ions is 1.44 times larger for the electrostatic run than that for the electromagnetic run, the final value differs by 1.08 times compared with the same time at 25 fs. Similarly, the electron energy is 1.07 times larger for the former than that for the latter.

5 Summary

Relativistic molecular dynamics were described using highly accurate interactions, to real charge and mass of particles. The Coulomb potential was collected in the infinite space, and the electromagnetic fields were calculated in the coordinate space. The longitudinal and transverse electric fields were separated as a good approximation because the physical process was contained essentially in 100 nm of the accelerated nanotube; the light travels over one-tenth of the period of an 800-nm sapphire laser in 0.3 fs.

As an application of the relativistic and electromagnetic simulation code, the nanotube accelerator was performed using the MPI implementation with 52 ranks by 16 processors (minimal case). With the $E \times B$ pulse of 800 nm, the positive ions were accelerated preferentially to the parallel direction of the nanotube. For $\geq 10^{20} \text{W/cm}^2$, the electrons became asymmetric in the perpendicular direction with 80% or more of the speed of light. The gold ions were partially ionized at $Z_{is} \geq 50$. The energy of the multilayer gold ions reached 30 MeV, and the energy efficiency of the gold ions to electrons was about 1% at 10^{22}W/cm^2 .

Finally, the electromagnetic field effects were examined in the electrostatic and electromagnetic codes. The chosen domain in the electromagnetic code was less than one period of 800-nm laser, which was satisfactory in the molecular dynamics simulation.

Acknowledgments

One of the authors (M.T.) would like to thank Professor A.Iiyoshi and Professor M.Sato for their kindness and discussions. The present simulations were performed using Fujitsu FX100 Supercomputer at National Institute for Fusion Science, Japan.

Appendix: Motion and Maxwell Field Equations by the International System of Units

The equation of motion for plasmas in the international system of units is written as.

$$d\vec{p}_i/dt = -\nabla \sum_{j=1}^N [q_i q_j / 4\pi\epsilon_0 r_{ij} + \Phi(r_i, r_j)] + q_i [\vec{E}_T(\vec{r}_i, t) + \vec{v}_i \times \vec{B}(\vec{r}_i, t)], \quad (\text{A.1})$$

$$d\vec{r}_i/dt = \vec{v}_i, \quad \vec{p}_i = m_i \vec{v}_i / \sqrt{1 - (\vec{v}_i/c)^2}. \quad (\text{A.2})$$

The $\Phi(r_i, r_j)$ is the short-range potential, the \vec{E}_T and \vec{B} are the transverse electric and magnetic fields, respectively, and $\mu_0 = 4\pi \times 10^{-7} \text{W/Am}$ and $\epsilon_0 = 1/\mu_0 c^2$. The Maxwell field equations are written as,

$$\nabla \cdot \vec{E}_L(\vec{r}, t) = (1/\epsilon_0) \sum_{i=1}^N q_i S(\vec{r} - \vec{r}_i), \quad (\text{A.3})$$

$$\partial \vec{B} / \partial t = -\nabla \times \vec{E}_T, \quad (\text{A.4})$$

$$\mu_0 \epsilon_0 \partial \vec{E}_T / \partial t = \nabla \times \vec{B} - \mu_0 \sum_{i=1}^N q_i \vec{v}_{T,i} S(\vec{r} - \vec{r}_i), \quad (\text{A.5})$$

$$\nabla \cdot \vec{B} = 0. \quad (\text{A.6})$$

The magnetic field is $\vec{B} = \mu_0 \vec{H}$ in plasmas. The symbol L is the longitudinal electric field, and the shape function $S(\vec{r})$ is prorated to nearest grids. The values are, $c = 2.998 \times 10^8 \text{m/s}$, $e = 1.602 \times 10^{-19} \text{C}$, $m_e = 9.1110 \times 10^{-31} \text{kg}$, and $1\text{eV} = 1.602 \times 10^{-19} \text{J}$.

References

- [1] S. S. Bulanov, A. Brantov, V. Yu. Bychenkov, V. Chvykov, G. Kalinchenko, T. Matsuoka, P. Rousseau, S. Reed, V. Yanovsky, D. W. Litzenberg, and A. Maksimchuk, *Med. Phys.*; 35 (2008) 1770.
- [2] T. Ditmire, J. Zweiback, V. P. Yanovsky, T. E. Cowan, G. Hays, and K. B. Wharton, *Nature*, 398 (1999) 489.
- [3] M. Roth, T. E. Cowan, M. H. Key, S. P. Hatchett, C. Brown, W. Fountain, J. Johnson, D. M. Pennington, R. A. Snavely, S. C. Wilks, K. Yasuike, H. Ruhl, P. Pegoraro, S. V. Bulanov, E. M. Campbell, M. D. Perry, and H. Powell, *Phys. Rev. Lett.*, 86 (2001) 436.
- [4] S. C. Wilks, A. B. Langdon, T. E. Cowan, M. Roth, S. Singh, S. Hatchett, M. H. Key, D. Pennington, A. MacKinnon, and R. A. Snavely, *Phys. Plasmas*, 8 (2001) 542.
- [5] T. E. Cowan, J. Fuchs, H. Ruhl, A. Kemp, P. Audebert, M. Roth, R. Stephens, I. Barton, A. Blazevic, E. Brambrink, J. Cobble, J. Fernandez, J. C. Gauthier, M. Geissel, M. Hegelich, J. Kaae, S. Karsch, G. P. Le Sage, S. Letzring, M. Manclossi, S. Meyroneinc, A. Newkirk, H. Pepin, and N. Renard-LeGalloudec, *Phys. Rev. Lett.*, 92 (2004) 204801.
- [6] B. M. Hegelich, B. J. Albright, J. Cobble, K. Flippo, S. Letzring, M. Paffett, H. Ruhl, J. Schreiber, R. K. Schulze, and J. C. Fernandez, *Nature*, 439 (2006) 441
- [7] H. Daido, M. Nishiuchi, and A. S. Pirozhkov, *Rep. Prog. Phys.*, 75 (2012) 056401.
- [8] M. Murakami and M. Tanaka, *Applied Phys. Letters*, 102 (2013) 163101.
- [9] Y. T. Kim, K. Ohshima, K. Higashimine, T. Uruga, M. Takata, H. Sue-matsu, and T. Mitani, *Angew. Chem., Int. Ed.*, 45 (2006) 407.
- [10] P. Mulser and D. Bauer, *High power laser-matter interaction*, Springer, Heidelberg, 2010, Chap.7.
- [11] M. Deserno and C. Holm, *J. Chem. Phys.* 109 (1998) 7694.
- [12] M. Tanaka, and M. Sato, *J. Chem. Phys.*, 126 (2007) 034509.
- [13] M. Tanaka, H. Kono, and K. Maruyama, *Phys. Review*, B79, (2009) 104420.
- [14] M. Tanaka and A. Yu. Grosberg, *J. Chem. Phys.*, 115 (2001) 567.
- [15] M. Tanaka and A. Yu. Grosberg, *Euro. Phys. J.*, E7 (2002) 371.
- [16] M. Tanaka, *Phys. Review*, E68 (2003) 061501.
- [17] Y. Rabin and M. Tanaka, *Phys. Rev. Letters*, 94 (2005) 148103.
- [18] M. Tanaka, A. Yu. Grosberg, V. S. Pande, and T. Tanaka, *Phys. Review*, E56 (1997) 5798.

- [19] M. Tanaka, J. Comput. Phys., 107 (1993) 124.
- [20] M. Tanaka, Phys. Plasmas, 3 (1996) 4010.
- [21] M. Murakami and M. Tanaka, Phys. Plasmas, 15 (2008) 082702.
- [22] L. D. Landau and E. M. Lifshitz, The Classical Theory of Fields, Fourth Revised English Edition, Course of Theoretical Physics volume 2, Butterworth Heinemann, New York, 1987.
- [23] R. Heras, European J. Physics, 38 (2017) 055203.
- [24] R. Courant, K. Friedrichs, and H. Levy, IBM J. Res. Develop., 11 (1967 [1928]) 215.